Effective tight-binding model for MX_2 under electric and magnetic fields

K. V. Shanavas[*]

Materials Science and Technology Division, Oak Ridge National Laboratory, Oak Ridge, Tennessee 37831-6056, USA

S. Satpathy

Department of Physics, University of Missouri, Columbia, Missouri 65221, USA

We present a systematic method for developing a five-band Hamiltonian for the metal d orbitals that can be used to study the effect of electric and magnetic fields on multilayer MX_2 ($M =$ Mo,W and $X =$ S,Se) systems. On a hexagonal lattice of d orbitals, the broken inversion symmetry of the monolayers is incorporated via fictitious s orbitals at the chalcogenide sites. A tight-binding Hamiltonian is constructed and then downfolded to get effective d-orbital overlap parameters using quasidegenerate perturbation theory. The steps to incorporate the effects of multiple layers, external electric and magnetic fields, are also detailed. We find that an electric field produces a linear-k Rashba splitting around the Γ point, while a magnetic field removes the valley pseudospin degeneracy at the $\pm K$ points. Our model provides a simple tool to understand the recent experiments on electric and magnetic control of valley pseudospin in monolayer dichalcogendies.

I. INTRODUCTION

Monolayers of transition-metal dichalcogenides having the formula MX_2 are in many ways similar to graphene and in recent years have shared some of its popularity. But, they also have crucial differences, such as metal d bands around the Fermi level, a direct band gap, and lack of inversion symmetry [1]. Presence of a band gap is highly desirable for electronics [2] and optoelectronics [3] applications, while transition-metal d orbitals lead to strong spin-orbit coupling (SOC) effects [4]. Coupled with lack of inversion symmetry, SOC leads to a large spin splitting of the valence bands at the corners (K points) in the Brillouin zone of the monolayers. Because of time-reversal symmetry, the splittings have opposite signs at K and $-K$ points, which gives rise to valley-dependent optical transitions [4]. This has been observed in MoS$_2$ with circularly polarized light [5,6], leading to potential valleytronics applications. Recently, control of the valley pseudospin via external magnetic fields is demonstrated experimentally, which works by breaking the degeneracy of energy states at $\pm K$ valleys [7,8].

Response of electronic states to external voltages has important consequences in the applications of these materials. Experimental measurements on bilayers of MoS$_2$ and WSe$_2$, which have intrinsic inversion symmetry, showed that gate voltages can tune valley magnetic moment and exciton splitting [9,10]. First-principles calculations on monolayers found that the band gaps are relatively stable against perpendicular electric fields [11,12], whereas in bilayers, electric fields cause a linear reduction in the band gap [13–15]. In both monolayers and bilayers, bands around Γ are spin degenerate and are susceptible to Rashba splitting under perpendicular field. Supercell calculations of MX_2 on Bi(111) heterostructures show giant Rashba splitting of the bands near Γ [16].

Tight-binding (TB) based model Hamiltonian approaches are ideally suited to study the effects of small perturbations such as electric fields on d-orbitals systems [17–19]. For MX_2, an effective two-band $k \cdot p$ model valid around K point has been widely used to study the transport, optical, and magnetic properties [4,20]. A good description of electronic structure in the entire zone requires explicitly including interaction between M-d and X-p orbitals within a tight-binding framework [21–23]. With the help of an effective three-band model derived from symmetry considerations, Liu *et al.* showed that interactions with up to three nearest neighbors are necessary for a good description of the bands around Fermi level in the monolayer systems [24].

In this paper, we develop an effective TB Hamiltonian containing M-d bands for monolayer and bilayer MX_2 and derive parameter values for MoS$_2$ and WS$_2$ by comparing with first-principles calculations and, in addition, study the effects of electric and magnetic fields on these systems using first-principles calculations and tight-binding models.

Our tight-binding method outlined in the subsequent sections is different from the earlier models in the sense that it is useful in cases where one is interested in a subset of the electronic states but the crystal structure has a lower symmetry than the subset. In the present case of a monolayer MX_2, for example, if one retains just the d orbitals and uses the standard tight-binding hopping integrals based on spherical symmetry around the atom (see, e.g., Ref. [25]), the Hamiltonian thus constructed will have an inversion symmetry with respect to a transition-metal atom, while the actual crystal structure does not have this symmetry, owing to the particular positions of the chalcogen atoms on either sides of the transition-metal plane. The situation can be remedied in two ways. One is to incorporate the full symmetry of the crystal into the hopping integrals between the orbitals using methods of group theory [24]. The second way, which we present here, is to add additional orbitals in the tight-binding theory, construct the Hamiltonian, and then remove these extra orbitals by Löwdin downfolding. The final TB Hamiltonian will be in the subspace that one is interested in and, yet, will have the proper symmetry of the structure. It is unimportant whether the extra orbitals added are real or fictitious, so long

_____

[*]kavungalvees@ornl.gov

as together they have the proper symmetry of the crystal. The empirical parameters of the effective Hamiltonian can be obtained by fitting to appropriate band structures, either experimental or theoretical. For the present case, we put s orbitals on the chalcogen sites as the additional orbitals. We thus provide here an intuitive method for deriving effective tight-binding Hamiltonian models which is quite general and can be extended to other materials.

II. METHODS

The first-principles calculations are carried out within density functional theory (DFT). Previous studies have reported that local density (LDA) and generalized gradient (GGA) approximations for exchange correlation yield similar results for geometry and electronic structure in MoS_2 [14]. Thus, in our calculations we use LDA within the projector augmented wave method as implemented in the Vienna *ab initio* simulation package [26]. An energy cutoff of 450 eV and k-space sampling on a $22 \times 22 \times 1$ grid are employed. The monolayered and bilayered systems are constructed by relaxing the bulk structure and adding a vacuum region of about 35 Å. The uniform electric field is simulated by adding a sawtoothlike potential to the Hamiltonian, similar to Ref. [19]. The chalcogen atoms are further relaxed under the electric field; however, their displacements are found to be small with a negligible effect on the electronic structure. The tight-binding models use a linear combination of atomic orbitals (LCAO) as the basis and Bloch functions to take the periodicity in the x and y directions. The Hamiltonian is parametrized in terms of the Slater-Koster overlap integrals such as $V_{dd\sigma}$, $V_{dd\pi}$, etc., which are fit by first-principles band structures.

This class of materials crystallizes most commonly in the $2H_b$ phase as shown in Fig. 1 for bulk MoS_2. They are made
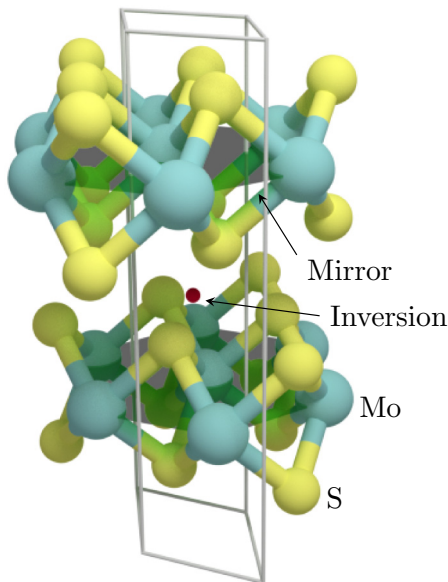
up of weakly bonded MX_2 layers, in which the metal ions M are coordinated trigonal prismatic fashion to the chalcogen ions X. As shown in Fig. 1, the monolayer has a mirror plane on the metal plane and has D_{3h} symmetry. The double layer on the other hand has an inversion center in the middle of the planes and thus has the point group D_{3d}.

III. RESULTS

A. Density functional results

Spin-orbit-coupled band structures from first-principles calculations for monolayers and bilayers of MoS_2 and WS_2 are presented in Fig. 2. As indicated by the orbital characters of the bands, the M-d states dominate close to the Fermi level while the S-p states lie below -1 eV. The absence of inversion symmetry in the case of monolayers removes the degeneracy at the K point resulting in the large spin-orbit splitting of the valence bands shown in red. The M-d_{z^2} bands around Γ point are spin degenerate in all cases, even though in bilayers interlayer coupling splits the two pairs. The band structures for MoS_2 and WS_2 are very similar, except for the larger spin-orbit coupling in W leads to a larger splitting of the bands at the K point.

The effect of perpendicular electric field on monolayer WS_2 from first-principles calculations is shown in Fig. 3, where the Rashba splitting of the valence bands near Γ point can be seen clearly. We find the spin splitting around Γ to be linearly proportional to the wave vector k as in the perovskite oxides with the form $\Delta_R = 2\alpha_R k$, where α_R is the Rashba parameter [19,27]. As we show in Sec. III B 6, this splitting arises because
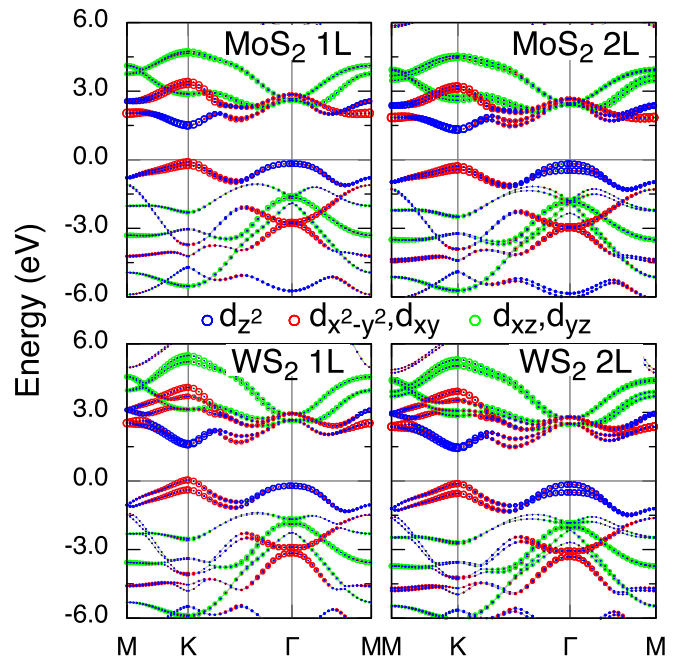

FIG. 1. (Color online) The $2H_b$-type crystallographic unit cell of MoS_2 contains two MoS_2 layers shifted by $(a/3, -a/3, c/2)$ from each other. A monolayer of MoS_2 contains a mirror plane whereas a double layer has an inversion point in the middle as shown.

FIG. 2. (Color online) The electronic band structures of monolayers (1L) and doublelayers (2L) of MoS_2 and WS_2 with spin-orbit coupling calculated using DFT without external electric field. The blue, red, and green symbols correspond to orbitals characters of d_{z^2}, $d_{x^2-y^2} + d_{xy}$, and $d_{xz} + d_{yz}$, respectively. The size of the symbols is proportional to the strength of the character.
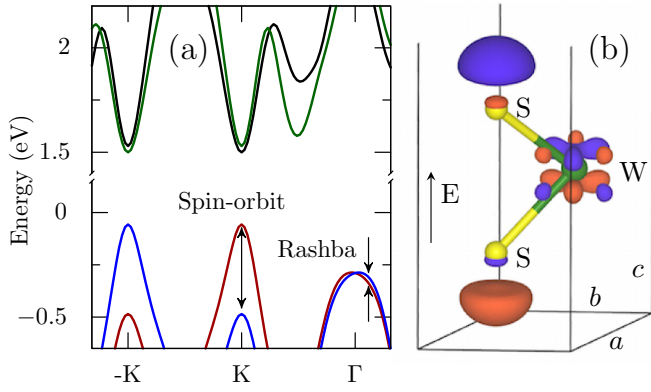
FIG. 3. (Color online) (a) Valence and conduction bands for WS$_2$ monolayer from DFT calculations with applied electric field of $E = 0.8$ eV/Å. The bands show linear Rashba spin splitting around the Γ point. (b) Change in charge density for WS$_2$ monolayer when electric field is applied ($\Delta\rho = \rho_0 - \rho_E$). The red and blue surfaces are for isovalues of $0.0006/\text{Å}^3$ and $-0.0006/\text{Å}^3$, respectively. The downward electric force on the electrons moves charge from the top S to the bottom one.
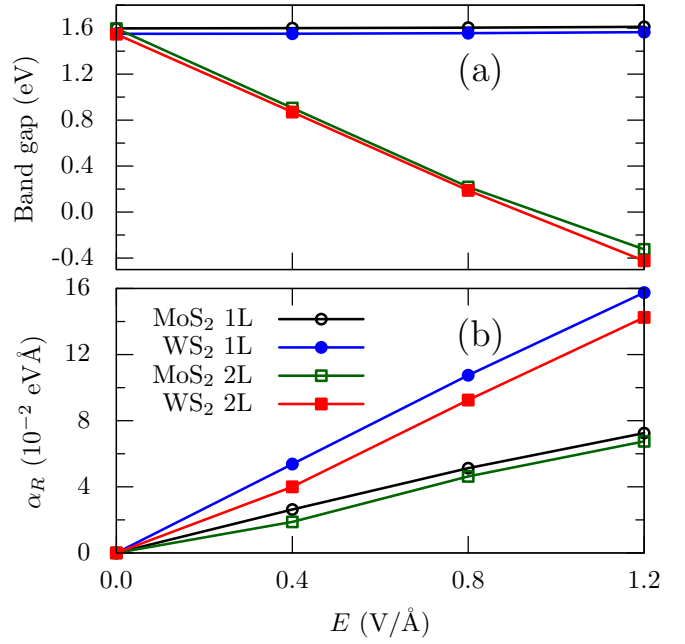

FIG. 4. (Color online) The variation of the (a) band gap and (b) Rashba parameter (α_R) in the valence bands near the Γ point as a function of electric field from first-principles calculations.

the electric field induced broken symmetry leads to coupling between d_{z^2} and d_{xz},d_{yz} orbitals. However, despite relative large applied field of 0.8 V/Å and the fact that the d_{xz},d_{yz} bands lie relatively close in energy (3 eV from Fig. 2), the splitting is rather small.

The change in charge density in monolayer WS$_2$ due to applied electric field is displayed in Fig. 3(b). The blue lobe above the top S atom denotes a reduction in charge density in that region while the red lobe indicates an enhancement. Thus, the electric field in $+z$ direction effectively transfers charge from the top S atom to the bottom one. However, this effect is quite small; adding up the charge above the W plane yields only $0.004e$. There is a similar redistribution of charge in the W-d orbitals. Note that the charge redistribution around chalcogen sites has full rotational symmetry about z, while the redistribution around transition-metal sites has only triangular symmetry.

Variation of the band gap for the different cases is shown in Fig. 4. In the case of monolayers, a field of 1 V/Å only slightly increases the band gap at the K point, by 13.5 and 14.6 meV for MoS$_2$ and WS$_2$, respectively. However, the gap reduces linearly in bilayers and disappears completely above 1 V/Å as shown in Fig. 4(a), in agreement with previous calculations [14,15]. The Rashba parameter α_R values for the d_{z^2} bands estimated from the DFT calculations are plotted in Fig. 4(b). Although smaller than the Zeeman-type splitting at K, the Rashba splitting is tunable by external electric field as shown in the figure.

B. Tight-binding model

In order to construct a tight-binding model for these systems, we proceed as follows. First, as will be explained in Sec. III B 1, we construct a 7×7 Hamiltonian for the monolayer containing M-d and X-s states and use Löwdin downfolding to derive a 5×5 matrix for the M-d states alone. In Sec. III B 2, we show how the electric field Hamiltonian can be derived by

following the same recipe, but starting from a slightly modified 7×7 Hamiltonian for the monolayer. The dominant effects of magnetic field are discussed in Sec. III B 3. For the bilayer, as discussed in Sec. III B 4, we start with a 14×14 matrix and downfold to a 10×10 effective model. The last component of the Hamiltonian, the spin-orbit coupling, is then included in Sec. III B 5 to construct the full Hamiltonian. Finally, 2×2 band Hamiltonians near high-symmetry points are derived in Sec. III B 6.

1. Monolayer (1L)

Since the bands near Fermi level are predominantly of M-d character, as can be seen from Fig. 2, we start with M-d orbitals on a hexagonal lattice for the tight-binding model. This system, however, has inversion symmetry, whereas the X ions above and below the metal plane break inversion in the monolayers. To get the proper symmetry of the system, s orbitals are placed at the X sites and a 7×7 tight-binding Hamiltonian following Harrison's recipe is constructed [25]. With the basis states $\phi_\alpha \equiv \{d_{z^2},d_{x^2-y^2},d_{xy},d_{xz},d_{yz},s_t,s_b\}$, where s_t,s_b are s orbitals at the top and bottom X sites, the Hamiltonian can be written as

$$H_{\text{TB}} = \begin{pmatrix} H_d & H_{sd} \\ H_{sd}^\dagger & H_s \end{pmatrix}. \tag{1}$$

The full expressions of the matrix elements in Eq. (1) are given in Appendix A.

Next, the fictitious s orbitals are removed by quasidegenerate perturbation theory and an effective Hamiltonian within the d-orbital basis is derived. We use the expression [28]

$$H_{\text{1L}} = H_d - \tfrac{1}{2}(H_{sd}\omega^\dagger + \omega H_{sd}^\dagger), \tag{2}$$

where the 5×2 matrix ω is calculated by solving the simultaneous equations $\omega H_s - H_d\omega = H_{sd}$, which, in the

present case, have 10 equations and 10 unknowns. Doing the math, we find that the effective Hamiltonian for the monolayer has the form

$$H_{1L} = \begin{pmatrix} h_1 & h_{12} & h_{13} & 0 & 0 \\ h_{12}^* & h_2 & h_{23} & 0 & 0 \\ h_{13}^* & h_{23}^* & h_3 & 0 & 0 \\ 0 & 0 & 0 & h_4 & h_{45} \\ 0 & 0 & 0 & h_{45}^* & h_5 \end{pmatrix}. \tag{3}$$

As we can see, Eq. (3) has the same nonzero matrix elements as H_d, but their k dependence is of different form as given in the following:

$$h_1 = \varepsilon_0 + t_1(2\cos\xi\cos\eta + \cos 2\xi),$$

$$h_2 = \varepsilon_1 + 2t_2\cos 2\xi + (t_2 + 3t_3)\cos\xi\cos\eta,$$

$$h_3 = \varepsilon_1 + 2t_3\cos 2\xi + (3t_2 + t_3)\cos\xi\cos\eta,$$

$$h_4 = \varepsilon_2 + 2t_4\cos 2\xi + (t_4 + 3t_5)\cos\xi\cos\eta,$$

$$h_5 = \varepsilon_2 + 2t_5\cos 2\xi + (3t_4 + t_5)\cos\xi\cos\eta,$$

$$h_{12} = t_6(\cos 2\xi - \cos\xi\cos\eta) + \sqrt{3}it_7\cos\xi\sin\eta,$$

$$h_{13} = -\sqrt{3}t_6\sin\xi\sin\eta + it_7(\sin 2\xi + \sin\xi\cos\eta),$$

$$h_{23} = \sqrt{3}(t_2 - t_3)\sin\xi\sin\eta - it_8\sin\xi(\cos\xi - \cos\eta),$$

$$h_{45} = \sqrt{3}(t_4 - t_5)\sin\xi\sin\eta - it_9\sin\xi(\cos\xi - \cos\eta).$$

The coordinates (ξ,η) are related to the reciprocal vectors via $\boldsymbol{k} = (k_x, k_y) = (2\xi/a, 2\eta/\sqrt{3}/a)$. The three onsite energies $\{\varepsilon_0, \varepsilon_1, \varepsilon_2\}$ and nine effective hopping parameters $\{t_1, t_2, t_3, t_4, t_5, t_6, t_7, t_8, t_9\}$ contain the effect of the s orbitals and are related to the Slater-Koster overlap integrals V_{dd}, V_{ds} as discussed in Appendix B.

Note that a three-band Hamiltonian extracted from H_{1L} for the orbitals d_{z^2}, $d_{x^2-y^2}$, and d_{xy} has the same form as that derived by Liu et al. based on symmetry for nearest-neighbor case [24]. As shown in Fig. 5, this effective five-band Hamiltonian can reproduce the d-band dispersions MX_2 monolayers compared to DFT. In the bands shown in Fig. 5,
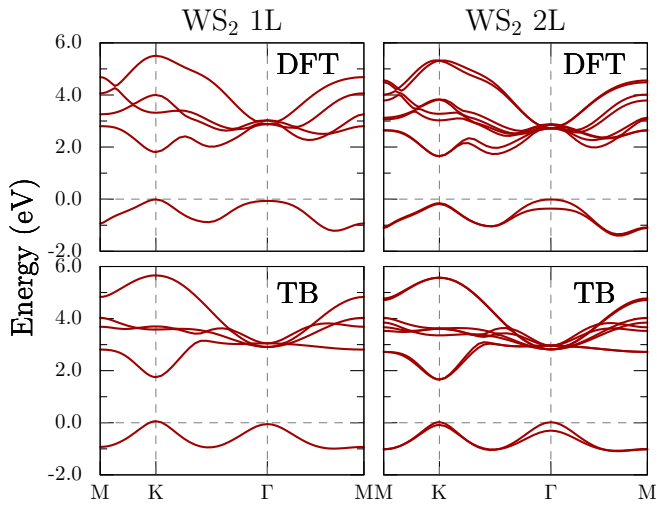
TABLE I. Parameters for the tight-binding model obtained by fitting to the DFT band-structure calculations. All energies are in 10^{-2} eV. The parameters $t_1 - t_9$ are hoppings and $\varepsilon_1 - \varepsilon_3$ are onsite energies in monolayers, while $v_1 - v_3$ are interlayer coupling for bilayers. The parameters $\Delta, \gamma_1, \gamma_2$ correspond to an electric field of $E = 0.8$ eV/Å.

	t_1	t_2	t_3	t_4	t_5	t_6	t_7	t_8	t_9
MoS$_2$	−37	90	105	22	135	6	−21	−6	−60
WS$_2$	−40	110	115	33	140	−7	−29	−9	80

	ε_1	ε_2	ε_3	v_1	v_2	v_3	Δ	γ_1	γ_2
MoS$_2$	105	218	360	0.9	0.2	0.5	120	20	5
WS$_2$	115	227	405	0.9	0.2	0.5	120	20	5

parameters obtained from fitting the model with DFT results are used which are listed in Table I.

The figure shows that the main features of the DFT are well reproduced by the tight-binding model, despite its simplicity. The figure also displays the bilayer case which will be discussed later in Sec. III B 4. For better agreement, such as the shape of the conduction band in the K-Γ-M direction, we have to go beyond the nearest-neighbor approximation and include more parameters [24]. In Appendix C, we derive a next-nearest-neighbor TB model for monolayer WS$_2$ which substantially improves the quality of the tight-binding band structure as shown in Fig. 8.

2. Electric field

Since the effect of perpendicular electric field is to add a z-dependent potential energy to the system, it can be incorporated through the onsite energies within the model. For the monolayer, if we fix the potential at the d orbitals to be zero, the onsite energies of bottom and top s orbitals become $\varepsilon_s - \delta$ and $\varepsilon_s + \delta$, respectively. Downfolding from the Hamiltonian in Eq. (1) with this modification, we find that the monolayer H has two parts:

$$H_{1L}^E = H_{1L} + H_E. \tag{4}$$

The term H_E is electric field induced and has the following form:

$$H_E = \begin{pmatrix} 0 & 0 & 0 & h_{14} & h_{15} \\ 0 & 0 & 0 & h_{24} & h_{25} \\ 0 & 0 & 0 & h_{34} & h_{35} \\ h_{14}^* & h_{24}^* & h_{34}^* & 0 & 0 \\ h_{15}^* & h_{25}^* & h_{35}^* & 0 & 0 \end{pmatrix}, \tag{5}$$

with

$$h_{14} = \sqrt{3}i\gamma_1(e^{i\eta}\sin\xi + 2\cos\xi\sin\xi),$$

$$h_{15} = \gamma_1(\cos 2\xi - \cos\xi\cos\eta + 3i\cos\xi\sin\eta),$$

$$h_{24} = 2\sqrt{3}i\gamma_2(-e^{i\eta}\sin\xi + \cos\xi\sin\xi),$$

$$h_{25} = \gamma_2(3 + \cos 2\xi - 4\cos\xi\cos\eta),$$

$$h_{34} = 6\gamma_2\sin^2\xi,$$

$$h_{35} = 2i\gamma_2(e^{-i\eta}\sin\xi + \sqrt{3}\cos\xi\sin\xi).$$

From the above expressions, we see that the electric field introduces two new parameters γ_1 and γ_2 to the monolayer

FIG. 5. (Color online) Comparison of TB and DFT bands without SOC and external potential for the monolayer and bilayer WS$_2$. Parameter values for the TB calculation are given in Table I.

Hamiltonian and leads to matrix elements that were formerly zero. In the case of the bilayer, in addition to the electric field term, we also need to take into account the potential difference between the two layers. For this, the onsite matrix elements of the M atom from the top layer are shifted by an additional energy Δ which is proportional to the distance between the layers and the strength of the electric field. Finally, within the tight-binding model, the electric field can also introduce new overlap parameters between d orbitals [19]. However, we find that the nonzero elements from these overlaps are the same as those in Eq. (5), but are much smaller in magnitude. Thus, we ignore them in the present analysis.

3. Magnetic field

The dominant effect of a magnetic field on the electronic structure of materials is the Zeeman effect, which lowers the energies of states with spins parallel to the field and raises energies of those antiparallel to it. The following Hamiltonian incorporates it in the model:

$$H_\text{B} = \mu \sigma_z \otimes \mathbb{1}_5, \tag{6}$$

where $\mathbb{1}_5$ is a 5×5 identity matrix, σ_z is the Pauli spin matrix, and the energy constant μ is proportional to the applied magnetic field $\mathbf{B}$ through $\mu = g\mu_B \mathbf{B}$, in which g is the gyromagnetic ratio of d orbitals ($g = 2$) and μ_B is the Bohr magneton. One of the higher-order effects not considered in the above model is the level splitting at the chalcogen sites, that may affect the hopping parameters within the d manifold. Secondly, similar to the electric field, the magnetic field also affects the hopping integrals through the vector potential $\mathbf{A}$, which can be expressed as $\tilde{t} = t \exp[-i e/\hbar \int dr \cdot \mathbf{A}(r,t)]$. For the energy scales of interest in this work, these effects are small and are hence ignored.

4. Bilayer (2L)

For multilayers we start with H_TB in Eq. (1) repeated to form a $7n \times 7n$ (where n is the number of layers) and allow coupling $V_{ss\sigma}$ between s_t and s_b orbitals from adjacent layers. Within the approximations that this coupling is weak and preserves symmetry, we can proceed as before and downfold using Eq. (2) to get $5n \times 5n$ matrix. For a bilayer ($n = 2$), we get

$$H_\text{2L} = \begin{pmatrix} H_\text{1L} & H_{12} \\ H_{12}^\dagger & H_\text{1L} \end{pmatrix}. \tag{7}$$

The matrix H_1L is the same as given in Eq. (3). The interlayer coupling matrix H_{12} has similar nonzero elements as H_1L, but has different k dependence as given as follows:

$$h_1 = 2\nu_1(3 + 4\cos\xi\cos\eta + 2\cos 2\xi),$$

$$h_2 = 3\nu_2(3 - 4\cos\xi\cos\eta + \cos 2\xi),$$

$$h_3 = 18\nu_2\sin^2\xi, \quad h_4 = -6\nu_3\sin^2\xi,$$

$$h_5 = \nu_3(-3 + 4\cos\xi\cos\eta - \cos 2\xi),$$

$$h_{12} = \sqrt{3}(\nu_1 + \nu_2)\{\cos 2\xi - \cos\xi(\cos\eta - 3i\sin\eta)\},$$

$$h_{13} = 3i(\nu_1 + \nu_2)(e^{i\eta} + 2\cos\xi)\sin\xi,$$

$$h_{23} = 6\sqrt{3}i\,\nu_2(\cos\xi - e^{i\eta})\sin\xi,$$

$$h_{45} = 2\sqrt{3}i\,\nu_3(\cos\xi - e^{-i\eta})\sin\xi.$$

Here, $\{\nu_1, \nu_2, \nu_3\}$ are interlayer coupling parameters, which arise from the interaction between d orbitals from adjacent layers. They are expected to be small, as the van der Waal's interaction responsible for this coupling is quite weak. Fitting to the bands from DFT calculations on bilayers, we get (in meV) $\nu = \{9.0, 2.0, 5.0\}$ for both MoS_2 and WS_2. Resulting band structures for the WS_2 case are compared with DFT in Fig. 5. The bands for MoS_2 are not shown since they are very similar.

5. Full Hamiltonian for d states

The final term that needs to be included is the spin-orbit coupling within the d orbitals of the form $H_\text{SO} = \lambda \mathbf{L} \cdot \mathbf{S}$, where λ is the spin-orbit parameter. With this, the full Hamiltonian for the monolayer and bilayer MX_2 can be written as

$$H_\text{1L}^\text{EB} = (H_\text{1L} + H_\text{E}) \otimes \mathbb{1}_2 + H_\text{B} + H_\text{SO}, \tag{8}$$

$$H_\text{2L}^\text{EB} = \begin{pmatrix} H_\text{1L}^\text{EB} & H_{12} \otimes \mathbb{1}_2 \\ H_{12}^\dagger \otimes \mathbb{1}_2 & H_\text{1L}^\text{EB} + \Delta\mathbb{1}_5 \end{pmatrix}. \tag{9}$$

From the DFT band structure, we find that the spin-orbit parameter for Mo-d orbitals is $\lambda_\text{Mo} = 0.08$ eV while that for W is $\lambda_\text{W} = 0.18$ eV. The other parameters γ and Δ are independent of the material, but depend on the strength of the electric field. We find that values of $\gamma/E = \{0.25, 0.063\}$ Å and $\Delta/E = 1.5$ Å give good fit to the DFT bands for both systems. The bands calculated for the WS_2 monolayers and bilayers for an electric field of $E = 0.8$ eV/Å and magnetic field induced splitting of $\mu = -0.1$ eV are shown in Fig. 6.

As expected, in bilayer WS_2 the degeneracy of the valence bands is lifted while the band gap reduces under applied electric field. It is driven by the parameter Δ, which shifts the electronic states from the layer at a higher potential to higher energies. On the other hand, in monolayer systems
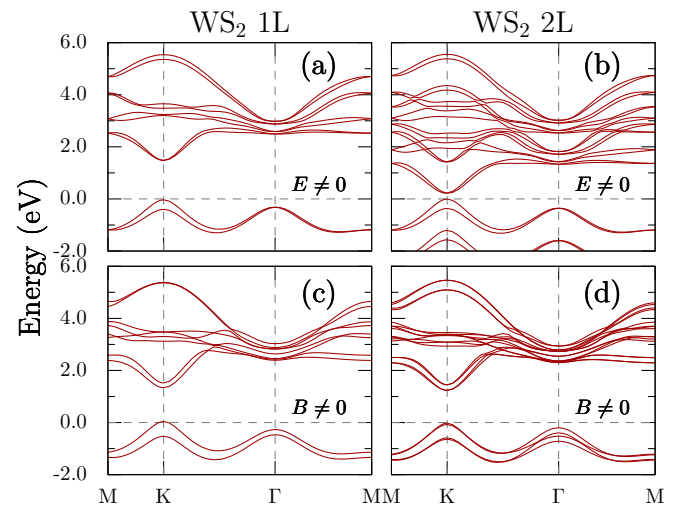

FIG. 6. (Color online) Band structure calculated using the tight-binding model in the presence of external electric and magnetic fields for WS_2 monolayers and bilayers with the parameters from Table I. For the finite electric field ($E \neq 0$) case (in electron volts) $\gamma_1 = 0.2$, $\gamma_2 = 0.05$, and $\Delta = 0.12$ are used, while for the finite magnetic field ($B \neq 0$) case $\mu = -0.1$ is used.
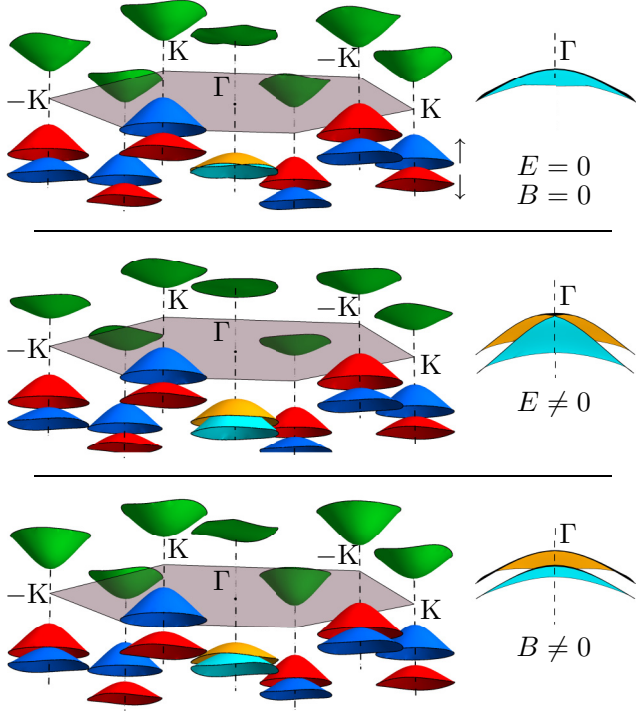
FIG. 7. (Color online) The conduction and valence bands of monolayer WS_2 calculated using tight-binding model in the 2D hexagonal Brillouin zone under finite electric field with $\gamma_1 = 0.2$, $\gamma_2 = 0.05$, and $\Delta = 0.12$ (middle panel) and finite magnetic field with $\mu = -0.1$ (bottom panel) are shown. Cross-sectional plots of the valence bands around Γ are shown in the right. Spin-orbit parameter is taken to be $2\lambda_W = 0.36$ eV to show the effects more clearly.

the spin splitting around K remains more or less unaffected. This is consistent with experimental observations that find a tunable field induced spin splitting in WSe_2 multiylayers and MoS_2 bilayers, but not in monolayers [9,10]. The magnetic field removes the degeneracy at Γ and enhances the splitting around K in both cases.

The effects of electric and magnetic fields on the bands near Fermi level calculated using the tight-binding Hamiltonian are shown in more detail in Fig. 7. Under zero field, the hexagonal two-dimensional (2D) Brillouin zone of the monolayer has a direct band gap at the zone corners $\pm K$. The valence bands at Γ are degenerate and have d_{z^2} character while those at $\pm K$ are spin split and of $d_{x^2-y^2}, d_{xy}$ type. Notice that the bands at K and $-K$ are spin flipped by the time-reversal symmetry. Under applied electric field, the degeneracy around Γ point is removed as a consequence of Rashba effect as can be seen from the cross-section plot in the middle panel of Fig. 7. The splitting has the familiar Mexican hat shape consistent with the calculations on $MoS_2/Bi(111)$ heterostructures [16].

The effects of magnetic field are shown in the bottom panel of Fig. 7. The band splitting near the Γ point is now independent of k under magnetic field and at K the splitting is enhanced, while it is reduced at $-K$, in agreement with experimental observations [7,8]. The band gap, on the other hand, reduces at K and increases at $-K$. The interactions

responsible for these behaviors are discussed in the next section.

6. 2×2 *Hamiltonians for monolayers around* Γ *and* K

It is possible to derive band Hamiltonians in the presence of electric and magnetic fields, near high-symmetry points such as Γ and K, for spin pairs following the recipe of Eq. (2) as long as bands are well separated from others. The resulting forms are often complex, but can be simplified further by expanding in k. Note that these Hamiltonians are only valid for the particular bands and k points, but are nevertheless useful to understand the interactions that are dominant in those regions. Diagonalizing the Hamiltonian in Eq. (3), we find that the valence bands near Γ are predominantly d_{z^2} in character. Downfolding the full Hamiltonian with the electric and magnetic field terms yields, in the basis $d_{z^2\uparrow}, d_{z^2\downarrow}$,

$$H^v(\Gamma) = \begin{pmatrix} \varepsilon + \mu + tk^2 & \alpha_R(ik_x + k_y) \\ -\alpha_R(ik_x - k_y) & \varepsilon - \mu + tk^2 \end{pmatrix}$$
$$= (\varepsilon + tk^2)\mathbb{1}_2 + \mu\sigma_z + \alpha_R(k_y\sigma_x - k_x\sigma_y), \quad (10)$$

where $k_\pm = k_x \pm ik_y$, $\varepsilon = \varepsilon_0 + 3t_1$, $t = -3t_1/2$, and $\alpha_R = 9\lambda\gamma_1/4(\varepsilon_0 - \varepsilon_2)$. Only the terms up to quadratic in k and linear in γ, λ are retained. The first term in Eq. (10) contains the onsite energy and the parabolic dispersion of the bands near zone center, the second one is the magnetic field induced spin splitting, and the last term is the Rashba coupling of the two spin states. Thus, in the absence of the magnetic field ($\mu = 0$), Eq. (10) reduces to the Rashba Hamiltonian. We can see that coupling through the electric field induced parameter γ_1 is responsible for the Rashba splitting, which corresponds to the coupling between d_{z^2} and d_{xz}, d_{yz} bands of the full Hamiltonian.

Around $\pm K$ points, the valence bands have wave functions $d_{x^2-y^2\uparrow} \mp id_{xy\uparrow}$ and $d_{x^2-y^2\downarrow} \mp id_{xy\downarrow}$, so first need to make a unitary transformation into this basis before the downfolding procedure [19]. Finally, we get:

$$H^v(K) = \begin{pmatrix} \varepsilon' + \mu - \lambda + t'k^2 & i\alpha' \\ -i\alpha' & \varepsilon' - \mu + \lambda + t'k^2 \end{pmatrix},$$
$$H^v(-K) = \begin{pmatrix} \varepsilon' - \mu - \lambda + t'k^2 & -i\alpha' \\ i\alpha' & \varepsilon' + \mu + \lambda + t'k^2 \end{pmatrix},$$

where $t' = 3/8(t_2 + t_3 + \sqrt{3}t_8/2)$, $\varepsilon' = \varepsilon_1 - 4t'$, and $\alpha' = (-6 + \sqrt{3})\gamma_2\lambda/2(\varepsilon_1 - \varepsilon_2)$. In condensed form,

$$H^v(\pm K) = \left(\varepsilon' + \frac{t'}{4}k^2\right)\mathbb{1}_2 - (\lambda \mp \mu)\sigma_z \pm \alpha'\sigma_x. \quad (11)$$

In the absence of any external fields, the valence bands are split by 2λ around $\pm K$ points. Interestingly, electric field induces a k-independent coupling between the up and down pseudospin channels proportional to the parameter γ_2, which will increase the splitting at K by about $10\gamma_2^2\lambda/(\varepsilon_1 - \varepsilon_2)$. However, this contribution is too small to be noticeable in Figs. 6 and 7. The magnetic field induced splitting, on the other hand, has opposite signs at $+K$ and $-K$, which breaks the symmetry of these points and results in the enhancement of splitting at K and reduction at $-K$ as shown in Fig. 7.

Deriving the 2×2 Hamiltonian for the conduction bands around $\pm K$, which has $d_{z^2\uparrow}, d_{z^2\downarrow}$ wave functions, we get

$$H^c(\pm K) = \varepsilon - \frac{3t_1}{2}\left(1 - \frac{k^2}{4}\right)\mathbb{1}_2 + \mu\sigma_z. \tag{12}$$

Thus, the magnetic field lifts the spin degeneracy of the conduction bands at $\pm K$ (Fig. 6), but does not break the symmetry between $+K$ and $-K$ points unlike in the valence bands. So, the change in band gap due to the magnetic field at $\pm K$ is $\Delta E_g = E_g(K) - E_g(-K) = -2\mu = -2g\mu_B B \approx -0.22 \times B$ meV, which compares well with charged exciton spectra measurements under magnetic field [7].

IV. CONCLUSIONS

In summary, we have developed a tight-binding model for the d orbitals of transition-metal dichalcogenides that contain the effect of chalcogenide ions through effective overlap parameters. We showed that this model can be easily extended to include multiple layers and the effect of external electric and magnetic fields. Within the nearest-neighbor approximation, the model is shown to have good agreement with first-principles calculations within DFT. The bands around Γ point develop a linear Rashba spin splitting when subjected to the electric fields. Further, in the case of bilayers, the potential difference between the two layers leads to a linear collapse of the band gap as the field is increased. The magnetic field lifts the valley pseudospin degeneracy at $+K$ and $-K$ points by shifting the bands in opposite direction at the two points with respect to the spin-orbit coupling.

ACKNOWLEDGMENTS

APPENDIX A: FULL MONOLAYER TB HAMILTONIAN

For the monolayer case, the full Hamiltonian of Eq. (1) can be written as

$$H_{\text{TB}} = \begin{pmatrix} d_1 & d_{12} & d_{13} & 0 & 0 & s_1 & s_1 \\ d_{12}^* & d_2 & d_{23} & 0 & 0 & s_2 & s_2 \\ d_{13}^* & d_{23}^* & d_3 & 0 & 0 & s_3 & s_3 \\ 0 & 0 & 0 & d_4 & d_{45} & -2s_3 & 2s_3 \\ 0 & 0 & 0 & d_{45}^* & d_5 & -2s_2 & 2s_2 \\ s_1^* & s_2^* & s_3^* & -2s_3^* & -2s_2^* & \varepsilon_s & 0 \\ s_1^* & s_2^* & s_3^* & 2s_3^* & 2s_2^* & 0 & \varepsilon_s \end{pmatrix}, \tag{A1}$$

where ε_s is the onsite energy of the s orbitals. Note that, due to the hexagonal symmetry, d_{xy} states have nonzero matrix elements with $d_{z^2}, d_{x^2-y^2}$ states, unlike in cubic perovskites where it couples with d_{xz}, d_{yz} states [19,29]. The nonzero matrix elements of the Hamiltonian are given below. We

use scaled reciprocal coordinates $\xi = k_x a/2$, $\eta = \sqrt{3}k_y a/2$, where a is the real-space lattice parameter:

$$d_1 = \varepsilon_0 + 2(V_0 + 3V_2)(2\cos\xi\cos\eta + \cos 2\xi),$$

$$d_2 = \varepsilon_1 + (3V_0 + 6V_1 + V_2)\cos\xi\cos\eta + 2(3V_0 + V_2)\cos 2\xi,$$

$$d_3 = \varepsilon_1 + 4V_1\cos 2\xi + (9V_0 + 2V_1 + 3V_2)\cos\xi\cos\eta,$$

$$d_4 = \varepsilon_2 + 4V_1\cos 2\xi + 2(V_1 + 6V_2)\cos\xi\cos\eta,$$

$$d_5 = \varepsilon_2 + 8V_2\cos 2\xi + (6V_1 + 4V_2)\cos\xi\cos\eta,$$

$$d_{12} = 2\sqrt{3}(V_0 - V_2)(\cos\xi\cos\eta - \cos 2\xi),$$

$$d_{13} = 6(V_0 - V_2)\sin\xi\sin\eta,$$

$$d_{23} = \sqrt{3}(3V_0 - 2V_1 + V_2)\sin\xi\sin\eta,$$

$$d_{45} = -2\sqrt{3}(V_1 - 2V_2)\sin\xi\sin\eta,$$

$$s_1 = V_s e^{-\frac{i\eta}{3}}(e^{i\eta} + 2\cos\xi),$$

$$s_2 = \sqrt{3}V_s e^{-\frac{i\eta}{3}}(-e^{i\eta} + \cos\xi),$$

$$s_3 = -3i V_s e^{-\frac{i\eta}{3}}\sin\xi,$$

where ε_1, ε_2, and ε_3 are the three onsite energies. The onsite energies of $d_{x^2-y^2}$ and d_{xy} as well as d_{xz} and d_{yz} are the same due to symmetry. The parameters V_0, V_1, V_2, and V_s are related to the Slater-Koster overlap integrals

$$V_0 = \frac{V_{dd\sigma}}{4}, \quad V_1 = \frac{V_{dd\pi}}{2}, \quad V_2 = \frac{V_{dd\delta}}{4}, \quad V_s = \frac{V_{sd\sigma}}{4}.$$

APPENDIX B: EFFECTIVE HOPPING PARAMETERS FOR MONOLAYER HAMILTONIAN

The onsite energies $(\varepsilon_1 - \varepsilon_3)$ and hopping parameters $(t_1 - t_9)$ of the effective monolayer Hamiltonian H_{1L} in Eq. (3) are related to the Slater-Koster overlap integrals in the full tight-binding Hamiltonian of Eq. (1) via the following expressions:

$$\varepsilon_0 = \varepsilon_0 - \frac{3V_{ds\sigma}^2}{8(\varepsilon_s - \varepsilon_0)}, \quad \varepsilon_1 = \varepsilon_1 - \frac{9V_{ds\sigma}^2}{16(\varepsilon_s - \varepsilon_1)},$$

$$\varepsilon_2 = \varepsilon_3 - \frac{9V_{ds\sigma}^2}{4(\varepsilon_s - \varepsilon_2)},$$

$$t_1 = \frac{V_{dd\sigma}}{2} + \frac{3V_{dd\delta}}{2} - \frac{V_{sd\sigma}^2}{4(\varepsilon_s - \varepsilon_0)},$$

$$t_2 = \frac{3V_{dd\sigma}}{4} + \frac{V_{dd\delta}}{4} - \frac{3V_{sd\sigma}^2}{32(\varepsilon_s - \varepsilon_1)},$$

$$t_3 = V_{dd\pi} + \frac{9V_{sd\sigma}^2}{32(\varepsilon_s - \varepsilon_1)}, \quad t_4 = V_{dd\pi} + \frac{9V_{sd\sigma}^2}{8(\varepsilon_s - \varepsilon_2)},$$

$$t_5 = V_{dd\delta} - \frac{3V_{sd\sigma}^2}{8(\varepsilon_s - \varepsilon_2)},$$

$$t_6 = -\frac{\sqrt{3}V_{dd\sigma}}{2} + \frac{\sqrt{3}V_{dd\delta}}{2} + \frac{\sqrt{3}V_{sd\sigma}^2}{16(\varepsilon_s - \varepsilon_0)} + \frac{\sqrt{3}V_{sd\sigma}^2}{16(\varepsilon_s - \varepsilon_1)},$$

$$t_7 = \frac{3V_{sd\sigma}^2}{16(\varepsilon_s - \varepsilon_0)} + \frac{3V_{sd\sigma}^2}{16(\varepsilon_s - \varepsilon_1)},$$

$$t_8 = \frac{3\sqrt{3}V_{sd\sigma}^2}{8(\varepsilon_s - \varepsilon_1)}, \quad t_9 = -\frac{3\sqrt{3}V_{sd\sigma}^2}{2(\varepsilon_s - \varepsilon_2)}.$$

APPENDIX C: TIGHT-BINDING WITH NEXT-NEAREST-NEIGHBOR INTERACTIONS FOR MONOLAYER WS$_2$

From Fig. 5 we can see that the tight-binding model with only nearest-neighbor interactions captures the band dispersions of both conduction and valence bands around K reasonably well, but underestimates the effective mass of valence band and slope of the conduction bands around Γ. In this appendix, we show that including the next-nearest-neighbor interactions between M-d orbitals improves the quality of the fit.

The transition-metal atoms have six next-nearest neighbors at $\sqrt{3}a$ in the ab plane. Including the effect of these atoms in the tight-binding model, we write

$$H'_{1L} = H_{1L} + H'_d. \tag{C1}$$

We find that H'_d has the following nonzero matrix elements:

$$h_1 = (4c_1 + c_2)(V'_{dd\sigma} + 3V'_{dd\delta}),$$

$$h_2 = c_1(3V'_{dd\sigma} + 12V'_{dd\pi} + V'_{dd\delta}) + c_2(3V'_{dd\sigma} + V'_{dd\delta}),$$

$$h_3 = c_1(9V'_{dd\sigma} + 4V'_{dd\pi} + 3V'_{dd\delta}) + 4c_2V'_{dd\pi},$$

$$h_4 = 4c_1(3V'_{dd\pi} + V'_{dd\delta}) + 4c_2V'_{dd\delta},$$

$$h_5 = 4c_1(V'_{dd\pi} + 3V'_{dd\delta}) + 4c_2V'_{dd\pi},$$

$$h_{12} = \sqrt{3}(2c_1 - c_2)(V'_{dd\delta} - V'_{dd\sigma}),$$

$$h_{13} = 6s_1(V'_{dd\sigma} - V'_{dd\delta}),$$

$$h_{23} = \sqrt{3}s_1(-3V'_{dd\sigma} + 4V'_{dd\pi} - V'_{dd\delta}),$$

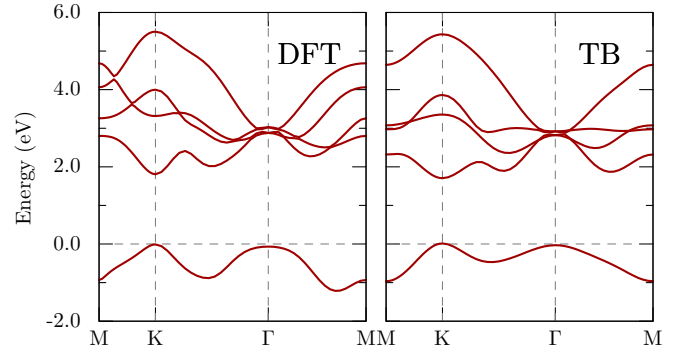$$h_{45} = \sqrt{3}s_1s_2(V'_{dd\delta} - V'_{dd\pi}),$$

FIG. 8. (Color online) Tight-binding model with second-neighbor coupling compared to DFT calculations of WS$_2$ monolayer. The full list of parameters are (in eV) $\varepsilon_1 = 0.4$, $\varepsilon_2 = 2.3$, $\varepsilon_3 = 3.7$, $t_1 = -0.01$, $t_2 = 0$, $t_3 = 0.03$, $t_4 = -0.4$, $t_5 = 0.05$, $t_6 = 0.8$, $t_7 = 0.75$, $t_8 = 0.83$, $t_9 = 0.8$, $V'_{dd\sigma} = 0.07$, $V'_{dd\pi} = 0.18$, and $V'_{dd\delta} = -0.09$.

where $4c_1 = \cos 3\xi \cos \eta$, $2c_2 = \cos 2\eta$, $4s_1 = \sin 3\xi \sin \eta$, and $s_2 = \sin \eta$. The primed overlap parameters indicate second-neighbor coupling. The resulting model Hamiltonian H'_{1L} is fitted to the DFT calculations on monolayer WS$_2$ and is shown in Fig. 8.

As we can see, this model correctly reproduces the dispersion of the conduction bands around the Γ point and the dip in the bands in the K-Γ direction. Note that we have not considered the second-neighbor interaction between the chalcogenide atoms. These atoms will also have second neighbors at $\sqrt{3}a$, and incorporating their effect may further improve the model.

[1] Z. Y. Zhu, Y. C. Cheng, and U. Schwingenschlögl, Phys. Rev. B **84**, 153402 (2011).

[2] B. Radisavljevic, A. Radenovic, J. Brivio, V. Giacometti, and A. Kis, Nat. Nanotechnol. **6**, 147 (2011).

[3] Q. H. Wang, K. Kalantar-Zadeh, A. Kis, J. N. Coleman, and M. S. Strano, Nat. Nanotechnol. **7**, 699 (2012).

[4] D. Xiao, G.-B. Liu, W. Feng, X. Xu, and W. Yao, Phys. Rev. Lett. **108**, 196802 (2012).

[5] T. Cao, G. Wang, W. Han, H. Ye, C. Zhu, J. Shi, Q. Niu, P. Tan, E. Wang, B. Liu, and J. Feng, Nat. Commun. **3**, 887 (2012).

[6] K. F. Mak, K. He, J. Shan, and T. F. Heinz, Nat. Nanotechnol. **7**, 494 (2012).

[7] D. MacNeill, C. Heikes, K. F. Mak, Z. Anderson, A. Kormányos, V. Zólyomi, J. Park, and D. C. Ralph, Phys. Rev. Lett. **114**, 037401 (2015).

[8] G. Aivazian, Z. Gong, A. M. Jones, R.-L. Chu, J. Yan, D. G. Mandrus, C. Zhang, D. Cobden, W. Yao, and X. Xu, Nat. Phys. **11**, 148 (2015).

[9] S. Wu, J. S. Ross, G.-B. Liu, G. Aivazian, A. Jones, Z. Fei, W. Zhu, D. Xiao, W. Yao, D. Cobden, and X. Xu, Nat. Phys. **9**, 149 (2013).

[10] H. Yuan, M. S. Bahramy, K. Morimoto, S. Wu, K. Nomura, B.-J. Yang, H. Shimotani, R. Suzuki, M. Toh, C. Kloc *et al.*, Nat. Phys. **9**, 563 (2013).

[11] Q. Yue, S. Chang, J. Kang, X. Zhang, Z. Shao, S. Qin, and J. Li, J. Phys.: Condens. Matter **24**, 335501 (2012).

[12] N. Zibouche, P. Philipsen, T. Heine, and A. Kuc, Phys. Chem. Chem. Phys. **16**, 11251 (2014).

[13] A. Ramasubramaniam, D. Naveh, and E. Towe, Phys. Rev. B **84**, 205325 (2011).

[14] Q. Liu, L. Li, Y. Li, Z. Gao, Z. Chen, and J. Lu, J. Phys. Chem. C **116**, 21556 (2012).

[15] N. Zibouche, P. Philipsen, A. Kuc, and T. Heine, Phys. Rev. B **90**, 125440 (2014).

[16] K. Lee, W. S. Yun, and J. D. Lee, Phys. Rev. B **91**, 125420 (2015).

[17] Z. Zhong, A. Tóth, and K. Held, Phys. Rev. B **87**, 161102 (2013).

[18] G. Khalsa, B. Lee, and A. H. MacDonald, Phys. Rev. B **88**, 041302 (2013).

[19] K. V. Shanavas, Z. S. Popović, and S. Satpathy, Phys. Rev. B **90**, 165108 (2014).

[20] Z. Gong, G.-B. Liu, H. Yu, D. Xiao, X. Cui, X. Xu, and W. Yao, Nat. Commun. **4**, 2053 (2013).

[21] E. Cappelluti, R. Roldán, J. A. Silva-Guillén, P. Ordejón, and F. Guinea, Phys. Rev. B **88**, 075409 (2013).

[22] F. Zahid, L. Liu, Y. Zhu, J. Wang, and H. Guo, AIP Adv. **3**, 052111 (2013).

[23] H. Rostami, A. G. Moghaddam, and R. Asgari, Phys. Rev. B **88**, 085440 (2013).

[24] G.-B. Liu, W.-Y. Shan, Y. Yao, W. Yao, and D. Xiao, Phys. Rev. B **88**, 085433 (2013).

[25] W. A. Harrison, *Electronic Structure and the Properties of Solids: The Physics of the Chemical Bond* (Freeman, San Francisco, 1980).

[26] G. Kresse and J. Hafner, Phys. Rev. B **47**, 558 (1993); G. Kresse and J. Furthmüller, *ibid.* **54**, 11169 (1996).

[27] K. V. Shanavas and S. Satpathy, Phys. Rev. Lett. **112**, 086802 (2014).

[28] R. Winkler, *Spin-orbit Coupling Effects in Two-Dimensional Electron and Hole Systems* (Springer, New York, 2003).

[29] K. V. Shanavas, J. Electron Spectrosc. **201**, 121 (2015).